Journal of Alloys and Compounds Communications 10 (2026) 100171

Contents lists available at ScienceDirect

Journal of Alloys and Compounds Communications

journal homepage: www.sciencedirect.com/journal/jacomc

Study of defects in chlorine-doped Sb_2Se_3 single crystals by photoluminescence spectroscopy

N. Abbasi [a,*], J. Krustok [a], R. Kaupmees [a], M. Danilson [a], T.D.C. Hobson [b], J.D. Major [c], K. Durose [c], M. Kauk-Kuusik [a], M. Grossberg-Kuusk [a]

[a] Department of Materials and Environmental Technology, Tallinn University of Technology, Ehitajate tee 5, Tallinn 19086, Estonia
[b] Department of Materials, Mathematical, Physical and Life Sciences Division, University of Oxford, Oxford OX1 3PH, United Kingdom
[c] Department of Physics, Stephenson Institute for Renewable Energy, University of Liverpool, Liverpool L69 7ZF, United Kingdom

ARTICLE INFO

Keywords:
Antimony selenide
Photoluminescence
Chlorine doping
Defects

ABSTRACT

Chlorine doping has been shown to significantly affect the electrical and optical properties of antimony selenide (Sb_2Se_3), yet its impact on defect-related radiative recombination remains poorly understood. In this study, we investigated the influence of Cl doping on the defect structure of Sb_2Se_3 single crystals using temperature- and excitation power-dependent photoluminescence (PL) spectroscopy, in direct comparison with an undoped reference crystal. Two distinct PL bands were observed at low temperature ($T = 8$ K) for both crystals, located at 0.84 eV (D1) and 1.09 eV (D2) in this n-type Cl-doped Sb_2Se_3, while undoped Sb_2Se_3 demonstrated PL bands at 0.89 eV (U1) and 1.02 eV (U2). The higher energy PL band at 1.09 eV (D2) is attributed to deep donor–deep acceptor (DD–DA) pair recombination, supported by its low thermal activation energy (42 ± 7 meV) and rapid quenching with increasing temperature. In contrast, the lower-energy PL band at 0.84 eV (D1) showed complex behavior, including a blueshift and a negative thermal quenching at low temperatures. This unique thermal and spectral behavior, which is absent in the undoped reference material, unequivocally links the recombination pathway to the extrinsic dopant. This emission is assigned to donor–acceptor pair recombination involving a deep acceptor and a Cl-induced shallow donor, likely corresponding to a Cl_{Se} antisite defect as predicted previously by density functional theory calculations. These findings contribute to an improved understanding of the effect of external doping on this promising inorganic absorber material, Sb_2Se_3, for photovoltaic applications.

1. Introduction

Antimony selenide (Sb_2Se_3) is a binary quasi-one-dimensional (Q1D) semiconductor that has attracted considerable attention as an absorber material for thin-film photovoltaic devices. Currently, Sb_2Se_3-based thin-film solar cells have achieved efficiencies approaching 11%, which remain roughly one-third of the detailed balance limit predicted by Shockley and Queisser (~30%) [1,2]. The material crystallizes in a stable orthorhombic structure and consists of earth-abundant elements. It exhibits a high absorption coefficient ($>10^5$ cm^{-1}) in the visible spectral region and a long minority carrier lifetime (~60 ns) [3–5], and a direct bandgap ($E_{g,d}$) of 1.17 eV at 300 K [6]. In addition, its resistance to moisture, oxygen, and ultraviolet radiation enhances its suitability for long-term photovoltaic operation [7].

Nevertheless, device performance is limited by a pronounced open-circuit voltage (Voc) deficit relative to established photovoltaic technologies. This limitation originates from the complex intrinsic defect chemistry and unconventional defect physics associated with the quasi-one-dimensional van der Waals structure of Sb_2Se_3. These effects manifest as low hole concentrations (~10^{13} cm^{-3}) and significant band tailing, reflected in a relatively large Urbach energy (~40 meV) [4]. The intrinsic defect landscape of Sb_2Se_3 involves point defects forming on the crystallographically inequivalent selenium (Se_1, Se_2, Se_3) and antimony (Sb_1, Sb_2) lattice sites. Among these, antisite configurations, specifically Sb occupying Se sites (Sb_{Se}) and Se occupying Sb sites (Se_{Sb}), are frequently reported as dominant deep-level defects. In addition to bulk point defects, recombination losses may also arise from grain boundaries and electrically active states located within the depletion region of the device [8,9]. In addition to intrinsic defects, extrinsic impurities introduced during synthesis can generate additional point defects and interact with the native defect landscape of Sb_2Se_3 [10–12]. Experimentally reported carrier concentrations typically lie in the range of

---

* Corresponding author.
E-mail address: nafiseh.abbasi@taltech.ee (N. Abbasi).

https://doi.org/10.1016/j.jacomc.2026.100171
Received 5 February 2026; Received in revised form 10 February 2026; Accepted 2 March 2026

$\sim 10^{13}$ cm^{-3} [13] to $\sim 10^{14}$ cm^{-3} [14], suboptimal for high-performance thin-film absorbers. The correspondingly low electrical conductivity ($\sim 10^{-6}$ Ω^{-1}.m^{-1}) limits device performance, motivating the use of intentional doping strategies to tailor the electronic properties. Although Sb_2Se_3 is generally regarded as a p-type semiconductor, instances of n-type conductivity have also been reported [15,16].

Controlling the carrier concentration in Sb_2Se_3 has therefore motivated the investigation of extrinsic dopants in addition to intrinsic defect engineering. Shalvey *et al.* [10] systematically compared cadmium and zinc as p-type dopants in Sb_2Se_3 single crystals and thin films. Although both elements successfully induced p-type conductivity in Sb_2Se_3, Cd proved significantly more effective, yielding lower resistivity and avoiding compensation over a wider concentration range. In contrast, Zn was effective only within a narrow doping window due to strong self-compensation effects. Cd-doped thin films enabled hole densities exceeding 10^{16} cm^{-3}, revealing a new shallow Cd_{Sb} acceptor level at 22 meV, identified through photoluminescence and Arrhenius analysis. This shallow acceptor is compensated by a deeper intrinsic level around 389 meV, which limits the attainable free-carrier density. Importantly, the use of Cd-doped absorbers led to a V_{oc} increase of up to 60 mV in thermally evaporated thin-film devices, highlighting cadmium as an effective route for improving Sb_2Se_3 solar cell performance. Tin (Sn) has likewise been investigated as a p-type dopant for Sb_2Se_3. Incorporation of 0.1 at% Sn increases the electrical conductivity from 2.71×10^{-6} to 7.50×10^{-2} S·cm^{-1} and raises the hole concentration to approximately 2×10^{16} cm^{-3} [17]. An additional study by Uslu *et al.* [18] indicate that Sn incorporation modifies the electronic structure, lowering the work function and shifting the Fermi level toward the valence band maximum, consistent with enhanced p-type character.

In addition to Sn, several other elements have been investigated as potential dopants in Sb_2Se_3 [19]. In contrast, iron doping markedly enhances both electronic performance and photoactivity, increasing the hole concentration by approximately three orders of magnitude from 3.7×10^{16} cm^{-3} to 1.0×10^{19} cm^{-3}, and improving the fill factor and overall power conversion efficiency of the resulting devices. Tellurium has been shown to modify the Se/Sb stoichiometry, enabling controlled Se-rich or Sb-rich compositions while simultaneously passivating deep-level defects, as confirmed by deep-level transient spectroscopy [20]. Under Se-rich conditions, such passivation yields an absolute efficiency improvement of about 2% relative to undoped films. Additional studies report that Te incorporation enhances absorber quality by suppressing surface oxidation and promoting a favorable [hk1] crystallographic orientation, thereby facilitating improved carrier transport [21]. Lead has also been explored as a p-type dopant in Sb_2Se_3 thin films. Based on theoretical predictions of a low formation energy for the Pb_{Sb} acceptor ($\sim$0.15 eV ionization energy), Pb incorporation was shown to increase hole concentrations to $\sim 10^{16}$ cm^{-3}, a result supported by temperature-dependent conductivity measurements [22].

In contrast, chlorine incorporation has been associated with the emergence of n-type conductivity in Sb_2Se_3. Reported carrier concentrations reach values as high as $\sim 10^{18}$ cm^{-3}, accompanied by electron mobilities up to 7.63 cm^2.V^{-1}.s^{-1} [15,23,24]. Residual Cl impurities originating from precursor materials were identified as the source of this behavior. Intentional incorporation of Cl using $MgCl_2$ as a dopant precursor further confirmed its role in driving n-type conductivity in single crystals. Finally, Hobson *et al.* [25] emphasized that although Sb_2Se_3 is frequently regarded as intrinsically p-type, the conductivity type is not always explicitly verified in experimental studies.

Modifications in the defect structure of a semiconductor are directly reflected in its optical and electrical response. Among the available characterization techniques, photoluminescence (PL) spectroscopy provides direct insight into defect-related radiative transitions and recombination pathways. Grossberg *et al.* [26] indicated that at low temperature (T = 10 K), the PL spectra of Sb_2Se_3 polycrystals exhibited three bands at 0.94, 1.10, and 1.24 eV. The emission at 0.94 eV was attributed to close donor-acceptor pair (DAP) recombination, whereas the 1.24 eV emission was assigned to distant donor-acceptor pair recombination. The origin of the PL band at 1.10 eV was not conclusively clarified in that study. Near band-edge excitons and biexcitons have also been detected in Sb_2Se_3 microcrystals at T = 10 K using a pulsed UV laser as an excitation source [27,28]. Furthermore, Ag-doping of Sb_2Se_3 thin films resulted in four distinct PL bands at 0.829 eV, 0.947 eV, 1.046 eV, and 1.143 eV at T = 8 K, attributed to deep donor-deep acceptor (DD-DA) pair recombination [29].

In this study, temperature- and excitation power-dependent photoluminescence spectroscopy is employed to investigate how chlorine incorporation influences radiative recombination in Sb_2Se_3, an aspect that remains insufficiently understood. Density functional theory (DFT) calculations predict low formation energies of < 0.5 eV for the Cl_{Se} defect on all non-equivalent Se sites, introducing a shallow donor defect level at 0.025 eV below the conduction band minimum (CBM) [25,30,31]. The present PL study focuses on deliberately Cl-doped Sb_2Se_3 single crystals, which were grown as comparative samples for unintentionally Cl-doped n-type Sb_2Se_3 thin films demonstrating efficient isotype heterojunction solar cells by Hobson *et al.* [25]. An undoped reference crystal was analyzed in parallel to enable a direct comparison of intrinsic and dopant-induced emission features. This approach provides a clear basis for distinguishing radiative transitions arising from chlorine-related defects from those inherent to the material.

2. Experimental

Sb_2Se_3 single-crystal samples were grown by Hobson *et al.* [25] by a vertical Bridgman melt-growth method. High-purity metallic Sb (99.9999%, Alfa Aesar) and Se (99.999%, Alfa Aesar) precursors were used to synthesize the initial Sb_2Se_3 powder. Cl-doping was achieved by mixing $MgCl_2$ powder with undoped Sb_2Se_3 powder (which had previously been synthesized in-house from the metallic precursors) at a Cl:Se atomic ratio of 1×10^{-4}. This mixture was used as the feed material for the Bridgman single-crystal growth process. The crystal growth process was carried out in a vertical single-zone furnace, with the ampoule tip being held at the peak temperature point of 620 °C, slightly above the melting point of Sb_2Se_3 (611 °C). A lowering rate of 1.15 mm/h was maintained over 7 days, with a temperature gradient of 6 °C/cm. This process resulted in crystals of 3 cm in length, with the first 1.5 −2 cm being a large-grained polycrystalline, and the remaining section confirmed to be a single crystal. Samples used for subsequent characterization were cleaved from the Cl-doped part of the Sb_2Se_3 crystal. Further details of the sample fabrication process can be found in [25]. The hot probe method confirmed the n-type conductivity of the crystal under investigation. The reference undoped Sb_2Se_3 single crystal was grown using the identical vertical Bridgman melt-growth processes for the Cl-doped crystal, but without the addition of the doping source $MgCl_2$. The hot probe method confirmed p-type conductivity. This controlled methodology ensures that any differences in the resulting PL spectra between the two samples can be attributed to the effect of extrinsic Cl-doping rather than variations in growth conditions.

The elemental composition of the Sb_2Se_3 crystal was determined by Energy Dispersive X-ray spectroscopy (EDX) using a Zeiss Merlin high-resolution scanning electron microscope (HR-SEM) equipped with a Bruker EDX-XFlash 6/30 detector. Raman scattering was utilized to obtain the phase composition of the studied Cl-doped and undoped Sb_2Se_3 single crystals. A Horiba LabRam HR800 spectrometer with a 532 nm laser line with a power of 0.42 mW and a spot size of 10 μm in diameter, equipped with a multichannel CCD detection system in the backscattering configuration, was used for the measurements at room temperature. The crystal structure of the single crystals was determined by X-ray diffraction (XRD) using a Rigaku Ultima IV diffractometer with monochromatic Cu Kα1 radiation (λ = 1.5406 Å) at 40 kV and 40 mA operating with the silicon strip detector D/teX Ultra. The lattice constants were determined using the Rietveld refinement procedure by the Rigaku PDXL version 1.4.0.3 software.

Temperature-dependent PL measurements were carried out in the temperature region from 8 K to 300 K by using a closed-cycle helium cryostat (Janis CCS-150) and a LakeShore Model 335 temperature controller to control the temperature. The crystal was glued with cryogenic grease on a copper plate and mounted on the cold finger of the cryostat. The Cobolt 08-DPL continuous wave (CW) laser with a wavelength of 532 nm was utilized for the PL excitation. An optical chopper was applied to modulate the incident laser beam on the sample, allowing the separation of the PL signal from the background noise. The emitted light was conditioned using a cut-off low-pass filter and focused on the lateral entrance of the computer-controlled single grating (600 lines/mm) monochromator (f = 0.64 m) (Horiba Jobin Yvon FHR640). Luminescence was dispersed by the monochromator and detected by the Hamamatsu InGaAs photomultiplier tube. A Stanford SR810 DSP lock-in amplifier was used to amplify the signal. Neutral density filters were applied to alter the power of the incident laser beam for the laser power-dependent PL measurements at T = 8 K. The excitation power density varied in the range from 73.6 mW/cm^2 to 885.2 mW/cm^2.

Photoluminescence measurements were carried out on both the Cl-doped and undoped Sb_2Se_3 crystals, but the detailed temperature- and power-dependent study was performed exclusively on the Cl-doped material, with the undoped sample serving as a reference.

3. Results and discussion

3.1. Compositional and structural properties

EDX analysis revealed that both the undoped reference crystal and the Sb_2Se_3 crystal grown with $MgCl_2$-containing feed material resulted in a near-stoichiometric elemental composition, slightly Se-poor composition (40.3 at% of Sb and 59.7 at% of Se). As Cl was introduced at the doping level, its presence was confirmed by Secondary Ion Mass Spectrometry (SIMS) by Hobson *et al.* [25]. The presence of Mg was not detected in the material. This suggests that the Mg impurities segregated out during the crystal growth process, while the Cl was incorporated into the crystal. The XRD analysis revealed an orthorhombic crystal structure with the space group *Pnma* (ICDD 01–083–7430) for the undoped and the Cl-doped single crystal samples studied (see Fig. 1). The determined lattice parameters were a = 11.761 Å, b = 3.969 Å, and c = 11.610 Å. Note that *Pnma* is the standard setting of space group no. 62, consistent with the ICDD reference used here. Some studies on Sb_2Se_3 adopted an alternative setting of the same space group, *Pbnm*, for convenience in crystallographic comparisons [32].

Raman spectroscopy further confirmed the presence of Sb_2Se_3 with the characteristic Raman peaks for both crystals, with no detectable secondary phases in either sample (see Fig. 2). The peak at 255 cm^{-1} arises from the Sb_2O_3 phase, which may form on the sample surface due to storage and handling the sample under ambient conditions. The Raman spectra are in agreement with previous studies of Sb_2Se_3 [33,34].

These results (XRD and Raman) further confirm the phase purity of the investigated undoped and Cl-doped Sb_2Se_3 crystal, which has been independently verified to be single-crystalline by orientation analysis by Hobson *et al.* [25], in the initial study. The refined lattice parameters and phase purity for both samples indicate that the introduction of Cl at the doping level does not alter the bulk crystal framework.

These results confirm that the variations observed in subsequent optical measurements are due to defect-level modifications rather than structural changes or secondary phase formation.

3.2. Photoluminescence of Cl-doped Sb_2Se_3 crystal

The low-temperature (T = 8 K) PL spectrum of the undoped and Cl-doped Sb_2Se_3 crystals is presented in Fig. 3. The PL spectrum of the undoped crystal (Fig. 3) consists of two slightly asymmetric PL bands at 0.89 eV (U1) and at 1.02 eV (U2), while the PL spectrum of the doped crystal (Fig. 3.b) demonstrated bands at 0.84 eV (D1) and 1.09 eV (D2). The PL band at 1.09 eV (D2) has been studied in detail, as in previous studies, it was sandwiched between two other PL bands, complicating the fitting of the temperature and laser power-dependent PL spectra [26]. In this study, the asymmetric double-sigmoidal function was used for fitting the PL bands [35].

The temperature dependencies of the PL spectra of the undoped and Cl-doped Sb_2Se_3 crystals from 8 K to 300 K are presented in Fig. 4a and Fig. 4c. Much faster quenching of the U2 and D2 bands with increasing temperature compared to the deeper U1 and D1 bands is detected as seen in Fig. 4a and Fig. 4c. The D2 band is fully quenched by T = 100 K, while the D1 band remains detectable up to room temperature. Moreover, the D1 band first shows an increase in the PL band intensity before starting to gradually quench from T = 70 K (see Fig. 6). This low-

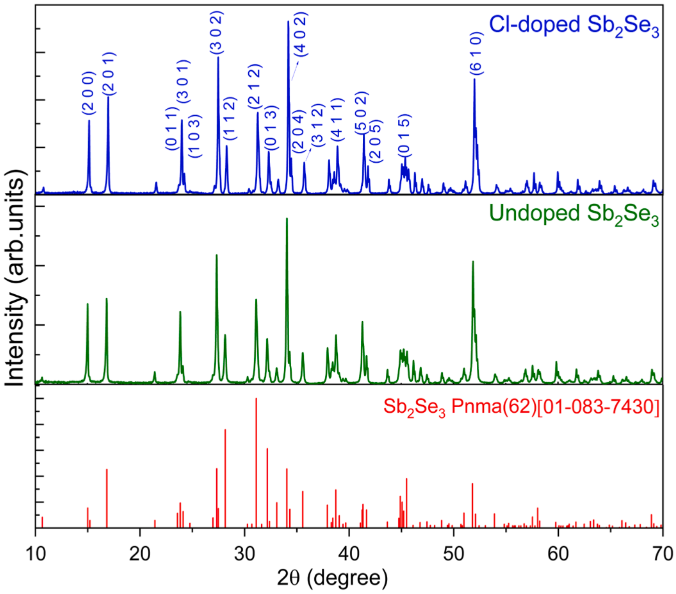

Fig. 1. The X-ray diffraction (XRD) data for the undoped and Cl-doped Sb_2Se_3 single crystals. The pattern confirms an orthorhombic crystal structure with space group *Pnma*, consistent with the reference (ICDD PDF No. 01–083–7430).

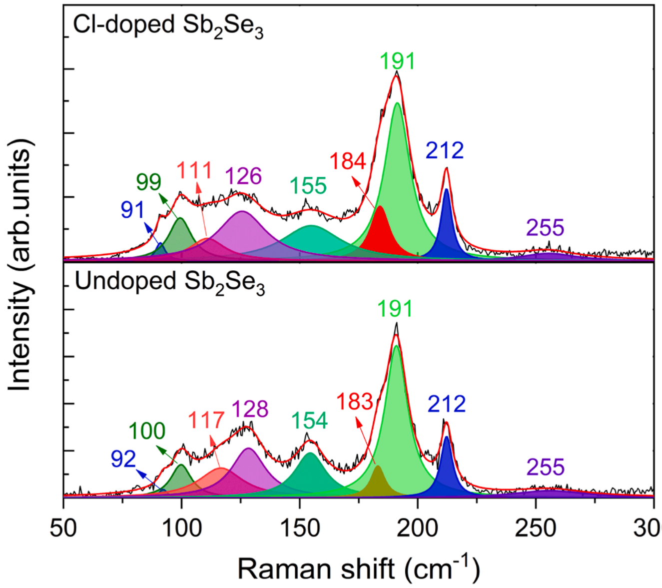

Fig. 2. Raman spectra of undoped and Cl-doped Sb_2Se_3 together with the fitting result using Lorentzian functions. A 532 nm laser line was used in the measurement.

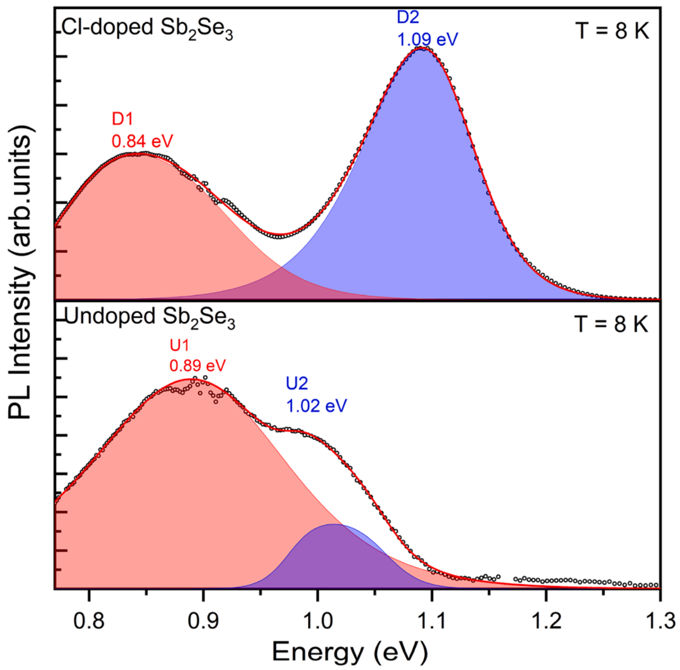

Fig. 3. Low-temperature PL spectra of the undoped and Cl-doped Sb_2Se_3 crystal, which were fitted using asymmetric double-sigmoidal functions.

temperature intensity increase (negative thermal quenching) is a key feature of the emission in the doped crystal. This unique phenomenon is absent in the corresponding low-energy band (U1) of the undoped reference crystal (Fig. 4d), which quenches continuously upon temperature increase. A redshift of the D2 band position E_{max-D2} with increasing temperature is detected from the fitting of the spectra, while the D1 band first shows a blueshift up to T = 100 K, followed by a redshift from T = 150 K until the room temperature (see Fig. 4b). The temperature dependence of the band gap $E_g(T)$ on Fig. 4b and Fig. 4d is taken from Ref. [36] allowing for distinguishing intrinsic band gap changes from defect-related emissions. Crucially, the corresponding band U1 in the undoped crystals (Fig. 4d) does not exhibit this blueshift, confirming that the negative thermal quenching of the D1 band of the Cl-doped sample at low temperatures can be attributed to external doping. Consequently, we focus on the detailed analysis of the D1 and D2 bands of the Cl-doped crystal.

The laser power dependence of the PL spectrum was measured at T = 8 K by varying the laser power density P from 73 mW/cm^2 to 885 mW/cm^2. Fig. 5a presents the dependence of the integrated intensity Φ of the PL bands on laser power density in a log-log scale, which follows the relation $\Phi \sim P^k$ [37]. The power coefficient values of $k = 0.6$ and $k = 0.7$ were found for the D1 and D2 bands, respectively, indicating radiative recombination involving charge carriers localized at defects within the band gap, consistent with earlier observations in kesterite- and tetrahedrite-based materials [38,39]. Both PL band positions E_{max} varied with increasing laser power and demonstrated blueshifts with magnitudes of 2.8 and 5.4 meV/decade for D1 and D2 bands, respectively (see Fig. 5b). The detected blueshift is a characteristic

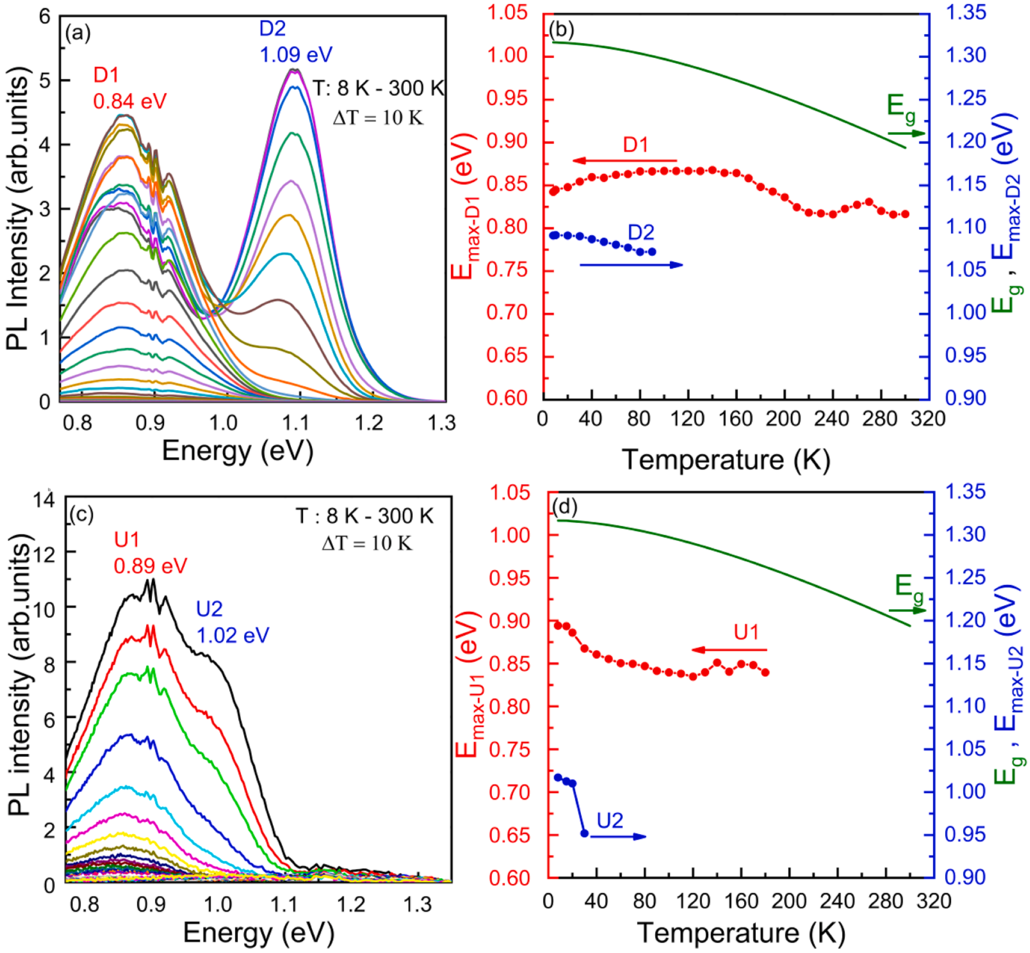

Fig. 4. (a), (c) The temperature dependencies of the PL spectra of the undoped and Cl-doped Sb_2Se_3 crystals, respectively. (b), (d). The temperature dependencies of the peak positions, E_{max} of the D1 and D2, U1 and U2 bands, respectively, together with the temperature dependence of the band gap E_g [36].

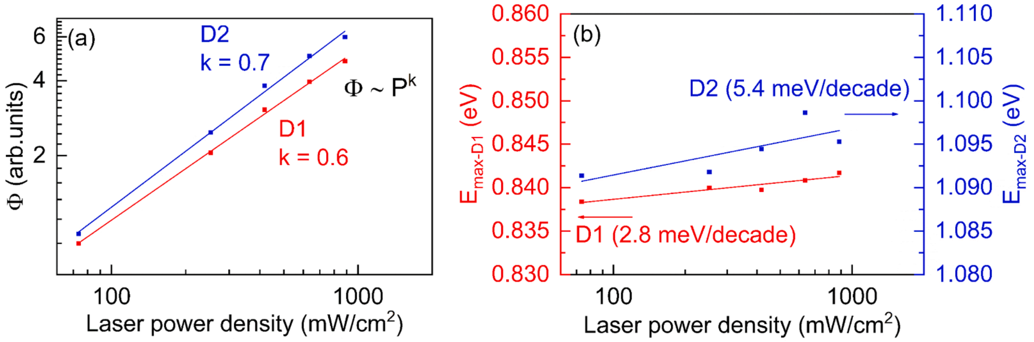

Fig. 5. (a) The integrated intensities (*Φ)* of D1 and D2 bands as a function of laser power (*P)* at T = 8 K on a log-log scale. (b) Laser power dependencies of the D1 and D2 bands' positions, E_{max}.

feature of donor-acceptor pair (DAP) recombination, which typically ranges between 2 and 7 meV per decade [40,41]. Fig. 6

From the temperature dependence of the integrated intensities Φ of the PL bands, the thermal activation energies, E_a, were determined. This is the place where the difference in thermal quenching comes out and proves the difference in the recombination mechanisms (Fig. 6). The Arrhenius plot is presented in Fig. 6, where the dependence of ln Φ (T) versus 1000/T of the D2 band was fitted by using the theoretical expression for discrete energy levels [42]:

$$\Phi\,(T) \quad = \quad \frac{\Phi\,(0)}{1 + \quad \alpha_1 T^{\frac{3}{2}} + \alpha_2 T^{\frac{3}{2}} \exp(-E_a/kT)} \tag{1}$$

where Φ is the integrated intensity, α_1 and α_2 are the process rate parameters and E_a is the thermal activation energy. According to the similar activation energies of U2 (E_a = 42 ± 7 meV) and D2 (E_a = 44 ± 3 meV), the same acceptor level is expected for them. However, since their positions differ, U2 at 1.02 eV and D2 at 1.09 eV, different donor levels are considered for them, meaning that the presence of Cl doping introduced another donor level for the D2 recombination, and not the same donor-acceptor pair recombination leads to these PL bands.

The significant difference between the thermal activation energies of U1 and D1 means their acceptor levels are different. In addition, D1 demonstrates negative thermal quenching that emphasizes various recombination mechanisms attributed to it, revealing the influence of Cl-doping. Hybrid DFT studies of intrinsic defects in Sb_2Se_3 were considered to identify the defects responsible for the U1 emission in the undoped crystal. Hybrid DFT calculations by Savory and Scanlon [43] show that under Sb-rich conditions, multiple charged defects, including amphoteric Sb_{Se} antisites and donor-like V_{Se} vacancies, coexist at the same Fermi-level position and strongly compensate one another. This coexistence implies a high probability of spatial defect correlation rather than the presence of isolated point defects. Consistent with this picture, Wijesinghe *et al.* [16] reported that under Sb-rich conditions, isolated Se_{Sb} shallow acceptors are thermodynamically unfavorable and that donor-type defects such as Sb_{Se} and V_{Se} dominate the intrinsic defect landscape. Nevertheless, experimental DLTS studies summarized in [16] reveal comparable concentrations of Sb_{Se} and Se_{Sb} antisites, suggesting the formation of correlated [Sb_{Se} + Se_{Sb}] defect complexes and vacancy pairing. When donor and acceptor defects form spatially correlated pairs, Coulomb interaction and local lattice relaxation can substantially reduce the effective ionization energy compared to isolated point defects, leading to a much smaller apparent thermal activation energy [26]. Because defect complexes can host electronic states that differ significantly from those of isolated defects and may exhibit shallower effective levels, we propose that donor–acceptor complexes, particularly Sb_{Se} + Se_{Sb} antisite pairs and V_{Se} + V_{Sb} vacancy pairs, represent the most plausible microscopic origin of the observed donor–acceptor-pair photoluminescence and the very small thermal activation energy. Therefore, in the following, we focus on the Cl-doped Sb_2Se_3 crystal and on the analysis of the recombination mechanisms associated with it, which are directly influenced by the presence of the extrinsic Cl dopant.

Considering the temperature and laser power dependencies of the D2 band, namely the blueshift with increasing laser power, fast quenching of the PL band with increasing temperature, and low thermal activation energy considering the distance of the D2 band from the low-temperature band gap energy of 1.32 eV of Sb_2Se_3, this emission results from the deep donor – deep acceptor (DD-DA) pair recombination rather than the previously proposed grain boundary-related recombination [34]. DD-DA pair recombination involving different deep donors and deep acceptors has been previously detected in several PL studies of Sb_2Se_3 [38,44]. This is supported by the DFT calculations predicting a high concentration of deep donor and acceptor defects in Sb_2Se_3, which

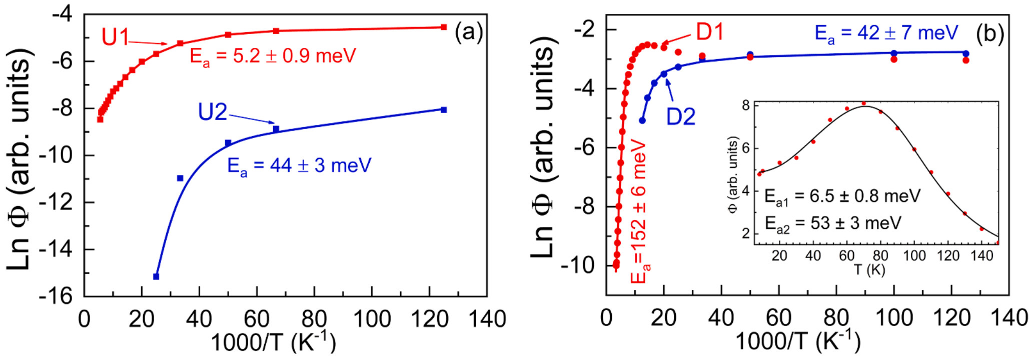

Fig. 6. The Arrhenius plot is used to determine the thermal activation energies of the PL bands for (a) undoped and (b) Cl-doped crystals. The inset graph in (b) presents the temperature dependence of the integrated intensity of the D1 band in the low-temperature region, fitted using Eq. (2). A different function, Eq. (1), was used to fit the high-temperature region of the D1 band. The fitting results are given as solid lines.

easily form deep donor-deep acceptor pairs [43].

As can be seen from the Arrhenius plot in Fig. 6, the D1 band shows negative thermal quenching at the low-temperature region (8 K – 70 K), which is followed by fast thermal quenching in the high-temperature region. Different theoretical functions were used for fitting the Arrhenius plot in the two different temperature regions. While Eq. (1) was used for the high-temperature region, the low-temperature region was fitted using the following formula [45]:

$$\Phi\,(T) \quad = \quad \frac{\Phi\,(0)(\quad 1 + \quad \alpha_1 exp\,(-E_{a1}/kT))}{1+\alpha_2 \exp(-E_{a2}/kT)}, \qquad (2)$$

where E_{a1} is the activation energy of the negative thermal quenching process, and E_{a2} represents the activation energy of non-radiative recombination. $E_{a1} = 6.5 \pm 0.8$ meV and $E_{a2} = 53 \pm 3$ meV were obtained from the fitting (see inset graph in Fig. 6). The thermal activation energy of $E_a = 152 \pm 6$ meV was found for the high-temperature quenching process. Considering the blueshift of the D1 band with increasing laser power (Fig. 5b), the behavior of the D1 band position with temperature (Fig. 4b) and the abnormal behavior of the D1 band intensity with temperature, we propose the following recombination model for the D1 band (presented in Fig. 7). According to this model, the recombination process is associated with strong band bending. In this scenario, the peak position $E_{max\text{-}D1}$ of the D1 emission at low temperatures is determined by the distance R of electrons from the center of the core, following a relationship similar to that observed in donor-acceptor (DA) pairs [42]: $E_{max} \sim 1/R$. At very low temperatures, electrons lack sufficient thermal energy to approach the core, resulting in a lower E_{max}. As the temperature increases, electrons gain enough energy to move closer to the core, leading to a rise in the peak position. Similar to DA pairs, the recombination probability ν of electrons and holes also depends on the distance R, following $\nu \sim \exp(-R)$. Consequently, the intensity of the D1 peak increases with temperature. At very low temperatures, recombination primarily occurs between holes at the acceptor sites and free electrons in the conduction band (Process A in Fig. 7). Due to the large separation distance R, the recombination probability for this process, and thus the intensity of the D1 band, is relatively low. As the temperature increases, electrons acquire sufficient thermal energy to move closer to the core, reducing the distance R. This leads to an increase in the D1 band intensity and a blueshift in the peak position $E_{max\text{-}D1}$ (Process B in Fig. 7). At temperatures $T \gtrsim 100$ K, the electrons have enough thermal energy to overcome the potential barrier, and donor-acceptor recombination (Process C in Fig. 7) becomes the dominant mechanism. Eventually, as the acceptor levels become depleted, thermal quenching of the PL emission occurs (Process D in Fig. 7). Similar models were proposed previously in CdTe [46], and in $CuGaTe_2$ [47,48]. The origin of these potential barriers and band bending can be related to the surface of the crystals, dislocations, grain boundaries, point-like clusters of acceptor defects or defect complexes. In heavily doped and compensated semiconductors, similar tail to impurity (TI) recombination is frequently observed, with a theoretical explanation provided years ago by Levanyuk and Ossipov [49].

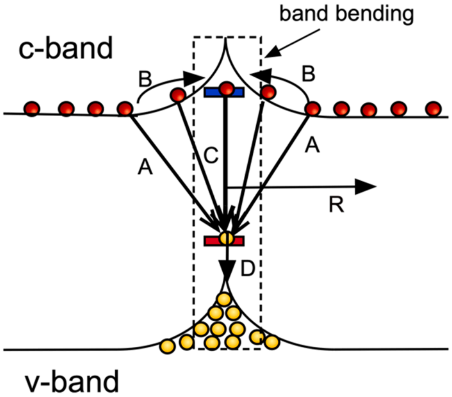

Fig. 7. Radiative recombination model for the D1 band of Cl-doped Sb_2Se_3 single crystal.

The $E_a = 152 \pm 6$ meV corresponds to the ionization energy of the acceptor defect. The shallow donor involved in the DAP recombination of the D1 band has not been previously observed in the PL studies of Sb_2Se_3. Considering that DFT calculations show low formation energies of < 0.5 eV for the Cl_{Se} defect on all non-equivalent Se sites introducing a shallow donor defect level at 0.025 eV below the CBM, we propose that the observed shallow donor is a Cl_{Se} antisite defect introduced to Sb_2Se_3 by Cl-doping using $MgCl_2$ as the chlorine source.

4. Conclusions

This work provides new insights into the impact of chlorine doping on the radiative recombination mechanisms in Sb_2Se_3 single crystals, validated through a direct comparison with an undoped reference crystal. While both crystals exhibited two distinct PL bands at low temperature (T = 8 K), their spectral positions and thermal behaviors differed. The undoped crystal showed bands at 0.84 eV (U1) and 1.02 eV (U2), whereas the Cl-doped crystal demonstrated bands at 0.84 eV (D1) and 1.09 eV (D2).

The 1.09 eV band (D2) is attributed to deep donor–deep acceptor (DD–DA) pair recombination. Its similar thermal activation energy to that of the corresponding undoped band (44 ± 3 meV for D2 and 42 ± 7 meV for U2) suggests the same acceptor levels are involved in both cases, while the difference in their positions indicates the different donor levels. In contrast, the characteristic blueshift and negative thermal quenching of 0.84 eV band (D1) are entirely absent in the corresponding undoped U1 band, which quenches continuously upon heating. This D1 emission is therefore assigned to band-bending influenced donor-acceptor pair recombination involving a deep acceptor with an ionization energy of 152 ± 6 meV and a Cl-induced shallow donor, most likely associated with the Cl_{Se} antisite defect.

The use of an undoped reference provides the necessary foundation to distinguish these extrinsic Cl-induced mechanisms from the material's intrinsic defect landscape. The identification of these Cl-induced shallow donor states suggests that Cl doping does not merely shift the conductivity type to n-type, as previously reported, but also enables new radiative recombination pathways for the light-induced charge carriers. These findings provide a clearer understanding of the interplay between extrinsic dopants and intrinsic defect states in Sb_2Se_3, offering a valuable foundation for tailoring its optoelectronic properties through controlled doping strategies.

CRediT authorship contribution statement

Nafiseh Abbasi: Conceptualization, Data curation, Methodology, Investigation, Formal analysis, Writing – original draft, Writing – review & editing. **Jüri Krustok:** Methodology, Writing – review & editing, Data analysis. **Reelika Kaupmees:** Methodology, Writing – review & editing, Formal analysis. **Mati Danilson:** Methodology, Data curation, Writing – review & editing. **Theodore D.C. Hobson:** Methodology, Data curation, Writing – review & editing. **Jonathan D. Major:** Methodology, Data curation, Writing – review & editing. **Ken Durose:** Methodology, Data curation, Writing – review & editing. **Marit Kauk-Kuusik:** Methodology, Formal analysis, Writing – review & editing. **Maarja Grossberg-Kuusk:** Conceptualization, Formal analysis, Writing – review & editing, Supervision, Resources, Funding acquisition.

Declaration of Competing Interest

The authors declare that they have no known competing financial interests or personal relationships that could have appeared to influence the work reported in this paper.

Acknowledgements

This work was supported by the Estonian Research Council [grant number PRG1023]; M-ERA.net project LightCell [grant number MNHA23040]; ERDF project GREENTECH [grant number TK210], and CETP project SUNLIFE [grant number Cetp-FP-2023–00137].

References

[1] Y. Zhao, S. Wang, L. Chuang, B. Che, X. Chen, H. Chen, R. Tang, X. Wang, G. Chen, T. Wang, J. Gong, T. Chen, X. Xiao, J. Li, Regulating deposition kinetics via a novel additive-assisted chemical bath deposition technology enables fabrication of 10.57%-efficiency Sb_2S_{e3} solar cells, Energy Environ. Sci. 15 (2022) 5118–5128, https://doi.org/10.1039/d2ee02261c.

[2] W. Shockley, H.J. Queisser, Detailed balance limit of efficiency of p-n junction solar cells, J. Appl. Phys. 32 (1961) 510–519, https://doi.org/10.1063/1.1736034.

[3] X. Liu, J. Chen, M. Luo, M. Leng, Z. Xia, Y. Zhou, S. Qin, D.J. Xue, L. Lv, H. Huang, D. Niu, J. Tang, Thermal evaporation and characterization of Sb_2Se_3 thin film for substrate Sb_2Se_3/CdS solar cells, ACS Appl. Mater. Interfaces 6 (2014) 10687–10695, https://doi.org/10.1021/am502427s.

[4] C. Chen, K. Li, J. Tang, Ten years of Sb_2Se_3 thin film solar cells, Sol. Rrl. 6 (2022) 2200094, https://doi.org/10.1002/solr.202200094.

[5] G. Liang, M. Chen, M. Ishaq, X. Li, R. Tang, Z. Zheng, Z. Su, P. Fan, X. Zhang, S. Chen, Crystal growth promotion and defects healing enable minimum open-circuit voltage deficit in antimony selenide solar cells, Adv. Sci. 9 (2022) 2105142, https://doi.org/10.1002/advs.202105142.

[6] C. Chen, W. Li, Y. Zhou, C. Chen, M. Luo, X. Liu, K. Zeng, B. Yang, C. Zhang, J. Han, J. Tang, Optical properties of amorphous and polycrystalline Sb_2Se_3 thin films prepared by thermal evaporation, Appl. Phys. Lett. 107 (2015) 043905, https://doi.org/10.1063/1.4927741.

[7] M.A. Bilya, A. Nabok, Y.P. Purandare, A.E. Alam, I.M. Dharmadasa, Growth and characterization of p-type and n-type Sb_2Se_3 for use in thin-film photovoltaic solar cell devices, Energ. (Basel) 17 (2024) 406, https://doi.org/10.3390/en17020406.

[8] M. Huang, P. Xu, D. Han, J. Tang, S. Chen, Complicated and unconventional defect properties of the quasi-one-dimensional photovoltaic semiconductor Sb_2Se_3, ACS Appl. Mater. Interfaces 11 (2019) 15564–15572, https://doi.org/10.1021/acsami.9b01220.

[9] A. Khadir, Performance investigation of Sb_2S_3 and Sb_2Se_3 earth abundant based thin film solar cells, Opt. Mater. (Amst.). 127 (2022) 112281, https://doi.org/10.1016/j.optmat.2022.112281.

[10] T.P. Shalvey, T.D.C. Hobson, F. Herklotz, R. Kaupmees, A.A. Almushawwah, B. G. Lewis, D.H. Christopher, S.R. Kavanagh, D. O.Scanlon, V. Dhanak, M. Grossberg-Kuusk, E. Lavrov, K. Durose, J.D. Major, Cadmium and Zinc-Doped p-type Sb_2Se_3 Single Crystals and Solar Cells, Adv. Energy Sustain. Res. (2025) e202500386, https://doi.org/10.1002/aesr.202500386.

[11] W. Tao, L. Zhu, K. Li, C. Chen, Y. Chen, Y. Li, X. Li, J. Tang, H. Shang, H. Zhu H, Coupled electronic and anharmonic structural dynamics for carrier self-trapping in photovoltaic antimony chalcogenides, Adv. Sci. 9 (2022) 2202154, https://doi.org/10.1002/advs.202202154.

[12] A. Mo, Y. Feng, B. Yang, W. Dang, X. Liang, W. Cao, Y. Guo, T. Chen, Z. Li, Controlling unintentional defects enables high-efficient antimony selenide solar cells, Adv. Funct. Mater. 34 (2024) 2316292, https://doi.org/10.1002/adfm.202316292.

[13] C. Chen, D.C. Bobela, Y. Yang, S. Lu, K. Zeng, C. Ge, B. Yang, L. Gao, Y. Zhao, M. C. Beard, J. Tang, Characterization of basic physical properties of Sb_2Se_3 and its relevance for photovoltaics, Front. Optoelectron 10 (2017) 18–30, https://doi.org/10.1007/s12200-017-0702-z.

[14] N. Spalatu, R. Krautmann, A. Katerski, E. Karber, R. Josepson, J. Hiie, I.O. Acik, M. Krunks, Screening and optimization of processing temperature for Sb_2Se_3 thin film growth protocol: interrelation between grain structure, interface intermixing and solar cell performance, Sol. Energy Mater. Sol. Cells 225 (2021) 111045, https://doi.org/10.1016/j.solmat.2021.111045.

[15] X. Luo, Y. Wang, D. Ren, R. Zhang, S. Chen, M. Cathelinaud, Y. Xu, X. Qiao, X. Zhang, X. Fan, Cl^{-1} doped Sb_2Se_3 polycrystals and films for optoelectric application, J. Solid State Chem. 324 (2023) 124115, https://doi.org/10.1016/j.jssc.2023.124115.

[16] U. Wijesinghe, G. Longo, O.S. Hutter, Defect engineering in antimony selenide thin film solar cells, Energy Adv. 2 (2022) 12–33, https://doi.org/10.1039/d2ya00232a.

[17] S. Chen, X. Qiao, Z. Zheng, M. Cathelinaud, H. Ma, X. Fan, X. Zhang, Enhanced electrical conductivity and photoconductive properties of Sn-doped Sb_2Se_3 crystals, J. Mater. Chem. C. 6 (2018) 6465–6470, https://doi.org/10.1039/c8tc01683f.

[18] M.E. Uslu, M. Danilson, K. Timmo, M. Grossberg-Kuusk, The effect of tin doping on the band structure and optical properties of polycrystalline antimony selenide, Phys. B Condens Matter 678 (2024) 415744, https://doi.org/10.1016/j.physb.2024.415744.

[19] M.B. Costa, F.W. de Souza Lucas, L.H. Mascaro, Electrodeposition of Fe-doped Sb_2Se_3 thin films for photoelectrochemical applications and study of the doping effects on their properties, J. Solid State Electrochem 22 (2018) 1557–1562, https://doi.org/10.1007/s10008-017-3768-z.

[20] Y. Ma, B. Tang, W. Lian, C. Wu, X. Wang, H. Ju, C. Zhu, F. Fan, T. Chen, Efficient defect passivation of Sb_2Se_3 film by tellurium doping for high performance solar cells, J. Mater. Chem. A. 8 (2020) 6510–6516, https://doi.org/10.1039/d0ta00443j.

[21] G. Chen, X. Li, M. Abbas, C. Fu, Z. Su, R. Tang, S. Chen, P. Fan, G. Liang, Tellurium doping inducing defect passivation for highly effective antimony selenide thin film Solar Cell, Nanomater. (Basel) 13 (2023) 1240, https://doi.org/10.3390/nano13071240.

[22] M. Huang, S. Lu, K. Li, Y. Lu, C. Chen, J. Tang, S. Chen, P-type antimony selenide via lead doping, Sol. Rrl. 6 (2022) 2100730, https://doi.org/10.1002/solr.202100730.

[23] F. Herklotz, E.V. Lavrov, T.D.C. Hobson, T. Shalvey, J.D. Major, K. Durose, Persistent photoconductivity in n-type Sb_2Se_3, Phys. Rev. Mater. 9 (2025) 084604, https://doi.org/10.1103/4b1m-yx1m.

[24] F. Herklotz, E.V. Lavrov, T.D.C. Hobson, J.D. Major, K. Durose, Charge carrier absorption in n-type Sb_2Se_3 (Sep), Appl. Phys. Lett. 125 (2024) 122104, https://doi.org/10.1063/5.0222193.

[25] T.D.C. Hobson, L.J. Phillips, O.S. Hutter, H. Shiel, J.E.N. Swallow, C.N. Savory, P. K. Nayak, S. Mariotti, B. Das, L. Bowen, L.A.H. Jones, T.J. Featherstone, M. J. Smiles, M.A. Farnworth, G. Zoppi, P.K. Thakur, T.L. Lee, H.J. Snaith, C. Leighton, D.O. Scanlon, V.R. Dhanak, K. Durose, T.D. Veal, J.D. Major, Isotype heterojunction solar cells using n-Type Sb_2Se_3 thin films, Chem. Mater. 32 (2020) 2621–2630, https://doi.org/10.1021/acs.chemmater.0c00223.

[26] M. Grossberg, O. Volobujeva, A. Penežko, R. Kaupmees, T. Raadik, J. Krustok, Origin of photoluminescence from antimony selenide, J. Alloy. Compd. 817 (2020) 152716, https://doi.org/10.1016/j.jallcom.2019.152716.

[27] J. Krustok, R. Kondrotas, R. Nedzinskas, K. Timmo, R. Kaupmees, V. Mikli, M. Grossberg, Identification of excitons and biexcitons in Sb_2Se_3 under high photoluminescence excitation density, Adv. Opt. Mater. 9 (2021) 2100107, https://doi.org/10.1002/adom.202100107.

[28] R. Kondrotas, R. Nedzinskas, J. Krustok, M. Grossberg, M. Talaikis, S. Tumėnas, A. Suchodolskis, R. Žaltauskas, R. Sereika, Photoreflectance and photoluminescence study of antimony selenide crystals, ACS Appl. Energy Mater. 5 (2022) 14769–14778, https://doi.org/10.1021/acsaem.2c02131.

[29] S. Polivtseva, O. Volobujeva, I. Kuznietsov, R. Kaupmees, M. Danilson, J. Krustok, P. Molaiyan, T. Hu, U. Lassi, M. Klopov, H. van Gog, A. M.A. van Huis, H. Kaur, A. Ivask, M. Rosenberg, N. Gathergood, C. Ni, M. Grossberg-Kuusk, Efficient defect-driven cation exchange beyond the nanoscale semiconductors toward antibacterial functionalization, ACS Appl. Mater. Interfaces 16 (2024) 62871–62882, https://doi.org/10.1021/acsami.4c11425.

[30] T.D.C. Hobson, L.J. Phillips, O.S. Hutter, K. Durose, J.D. Major, Defect properties of Sb_2Se_3 thin film solar cells and bulk crystals, Appl. Phys. Lett. 116 (2020) 261101, https://doi.org/10.1063/5.0012697.

[31] A. Stoliaroff, A. Lecomte, O. Rubel, S. Jobic, X.H. Zhang, C. Latouche, X. Rocquefelte, Deciphering the role of key defects in Sb_2Se_3, a promising candidate for chalcogenide-based solar cells, ACS Appl. Energy Mater. 3 (2020) 2496–2509, https://doi.org/10.1021/acsaem.9b02192.

[32] T.D.C. Hobson, K. Durose, Protocols for the Miller indexing of Sb_2Se_3 and a non-x-ray method of orienting its single crystals, Mater. Sci. Semicond. Process 127 (2021) 105691, https://doi.org/10.1016/j.mssp.2021.105691.

[33] P. Vidal-Fuentes, M. Guc, X. Alcobe, T. Jawhari, M. Placidi, A. Pérez-Rodríguez, E. Saucedo, V.I. Roca, Multiwavelength excitation Raman scattering study of Sb_2Se_3 compound: fundamental vibrational properties and secondary phases detection, 2D Mater. 6 (2019) 045054, https://doi.org/10.1088/2053-1583/ab4029.

[34] A. Shongalova, M.R. Correia, B. Vermang, J.M.V. Cunha, P.M.P. Salomé, P. A. Fernandes, On the identification of Sb_2Se_3 using Raman scattering, MRS Commun. 8 (2018) 865–870, https://doi.org/10.1557/mrc.2018.94.

[35] J. Krustok, H. Collan, M. Yakushev, K. Hjelt, The role of spatial potential fluctuations in the shape of the PL bands of multinary semiconductor compounds, Phys. Scr. T 79 (1999) 179–182, https://doi.org/10.1088/0031-8949/1999/T79/179.

[36] Y.P. Varshni, Temperature dependence of the energy gap in semiconductors, Physica 34 (1967) 149–154, https://doi.org/10.1016/0031-8914(67)90062-6.

[37] T. Schmidt, K. Lischka, W. Zulehner, Excitation-power dependence of the near-band-edge photoluminescence of semiconductors, Phys. Rev. B. 45 (1992) 8989–8994, https://doi.org/10.1103/PhysRevB.45.8989.

[38] N. Aihara, K. Tanaka, H. Uchiki, A. Kanai, H. Araki, Donor-acceptor pair recombination luminescence from monoclinic Cu_2SnS_3 thin film, Appl. Phys. Lett. 107 (2015) 032101, https://doi.org/10.1063/1.4927203.

[39] J. Krustok, T. Raadik, R. Kaupmees, F. Ghisani, K. Timmo, M. Altosaar, V. Mikli, M. Grossberg, Broad-band photoluminescence of donor-acceptor pairs in tetrahedrite $Cu_{10}Cd_2Sb_4S_{13}$ microcrystals, J. Phys. D Appl. Phys. 54 (2021) 105102, https://doi.org/10.1088/1361-6463/abce29.

[40] M.V. Yakushev, I. Forbes, A.V. Mudryi, M. Grossberg, J. Krustok, N.S. Beattie, M. Moynihan, A. Rockett, R.W. Martin, Optical spectroscopy studies of $Cu_2ZnSnSe_4$ thin films, Thin Solid Films 582 (2015) 154–157, https://doi.org/10.1016/j.tsf.2014.09.010.

[41] J. Krustok, R. Kaupmees, X. Li, M. Kauk-Kuusik, M. Grossberg, Detailed photoluminescence study of $Cu_2Ge(SSe)_3$ microcrystals, AIP Adv. 11 (2021) 085105, https://doi.org/10.1063/5.0053928.

[42] J. Krustok, H. Collan, K. Hjelt, Does the low-temperature Arrhenius plot of the photoluminescence intensity in CdTe point towards an erroneous activation energy? J. Appl. Phys. 81 (1997) 1442–1445, https://doi.org/10.1063/1.364955.

[43] C.N. Savory, D.O. Scanlon, The complex defect chemistry of antimony selenide, J. Mater. Chem. A. 7 (2019) 10739, https://doi.org/10.1039/c9ta02022e.

[44] M.E. Uslu, R. Kondrotas, R. Nedzinskas, O. Volobujeva, K. Timmo, M. Kauk-Kuusik, J. Krustok, M. Grossberg, Study of the optical properties of $Sb_2(Se_{1-x}S_x)_3$ (x = 0–1)

solid solutions, Mater. Sci. Semicond. Process 144 (2022) 106571, https://doi.org/10.1016/j.mssp.2022.106571.

[45] H. Shibata, Negative thermal quenching curves in photoluminescence of solids, Jpn. J. Appl. Phys. 37 (1998) 550–553, https://doi.org/10.1143/JJAP.37.550.

[46] J. Krustok, J. Mädasson, J. Hite, Photoluminescence properties of Z-bands in CdTe, Phys. Status Solidi A. 165 (1998) 517–521, https://doi.org/10.1002/(SICI)1521-396X(199802)165:23.0.CO;2-O.

[47] J. Krustok, J. Raudoja, M. Yakushev, R.D. Pilkington, H. Collan, Photoluminescence study of deep levels in $CuGaTe_2$ crystals, J. Appl. Phys. 86 (1999) 5305–5307, https://doi.org/10.1063/1.371517.

[48] A. Jagomägi, J. Krustok, M. Grossberg, M. Danilson, J. Raudoja, Deep defect related photoluminescence in heavily doped $CuGaTe_2$ crystals, Phys. Stat. Sol. A. 203 (2006) 949–955, https://doi.org/10.1002/pssa.200521118.

[49] A.P. Levanyuk, V.V. Osipov, Edge luminescence of direct-gap semiconductors, Sov. Phys. Usp. 24 (1981) 187–215, https://doi.org/10.1070/PU1981v024n03ABEH004770.